

## Plane shock loading on mono- and nano-crystalline silicon carbide

Paulo S. Branicio, Jingyun Zhang, José P. Rino, Aiichiro Nakano, Rajiv K. Kalia, and Priya Vashishta

Citation: *Appl. Phys. Lett.* **112**, 111909 (2018); doi: 10.1063/1.5025583

View online: <https://doi.org/10.1063/1.5025583>

View Table of Contents: <http://aip.scitation.org/toc/apl/112/11>

Published by the [American Institute of Physics](#)

---

### Articles you may be interested in

[Shock-induced microstructural response of mono- and nanocrystalline SiC ceramics](#)

*Journal of Applied Physics* **123**, 145902 (2018); 10.1063/1.5023915

[Comparison of microrings and microdisks for high-speed optical modulation in silicon photonics](#)

*Applied Physics Letters* **112**, 111108 (2018); 10.1063/1.5019590

[High-efficiency optical terahertz modulation of aligned Ag nanowires on a Si substrate](#)

*Applied Physics Letters* **112**, 111101 (2018); 10.1063/1.5008485

[Mechanical response of CH<sub>3</sub>NH<sub>3</sub>PbI<sub>3</sub> nanowires](#)

*Applied Physics Letters* **112**, 111901 (2018); 10.1063/1.5023115

[Temperature-dependent and optimized thermal emission by spheres](#)

*Applied Physics Letters* **112**, 111906 (2018); 10.1063/1.5010426

[Surface-initiated phase transition in solid hydrogen under the high-pressure compression](#)

*Applied Physics Letters* **112**, 111602 (2018); 10.1063/1.5012882

---

PHYSICS TODAY

WHITEPAPERS

### MANAGER'S GUIDE

Accelerate R&D with  
Multiphysics Simulation

READ NOW

PRESENTED BY

 COMSOL

## Plane shock loading on mono- and nano-crystalline silicon carbide

Paulo S. Branicio,<sup>1,2,a)</sup> Jingyun Zhang,<sup>3,4</sup> José P. Rino,<sup>5</sup> Aiichiro Nakano,<sup>2</sup> Rajiv K. Kalia,<sup>2</sup> and Priya Vashishta<sup>2</sup>

<sup>1</sup>Mork Family Department of Chemical Engineering and Materials Science, University of Southern California, Los Angeles, California 90089, USA

<sup>2</sup>Collaboratory for Advanced Computing and Simulations, Departments of Chemical Engineering and Materials Science, Physics and Astronomy, and Computer Science, University of Southern California, Los Angeles, California 90089, USA

<sup>3</sup>Jiangsu Key Laboratory for Optoelectronic Detection of Atmosphere and Ocean, Nanjing University of Information Science and Technology, Nanjing 210044, China

<sup>4</sup>School of Physics and Optoelectronic Engineering, Nanjing University of Information Science and Technology, Nanjing 210044, China

<sup>5</sup>Department of Physics, Universidade Federal de São Carlos, Rodovia Washington Luís, km 235, São Carlos, SP, Brazil

(Received 10 February 2018; accepted 28 February 2018; published online 15 March 2018)

The understanding of the nanoscale mechanisms of shock damage and failure in SiC is essential for its application in effective and damage tolerant coatings. We use molecular-dynamics simulations to investigate the shock properties of 3C-SiC along low-index crystallographic directions and in nanocrystalline samples with 5 nm and 10 nm grain sizes. The predicted Hugoniot in the particle velocity range of 0.1 km/s–6.0 km/s agrees well with experimental data. The shock response transitions from elastic to plastic, predominantly deformation twinning, to structural transformation to the rock-salt phase. The predicted strengths from 12.3 to 30.9 GPa, at the Hugoniot elastic limit, are in excellent agreement with experimental data. *Published by AIP Publishing.*

<https://doi.org/10.1063/1.5025583>

The outstanding mechanical properties of SiC make it a versatile material suitable for many applications including high-power high-temperature electronics,<sup>1,2</sup> abrasives,<sup>3</sup> gas turbines,<sup>4</sup> brake systems,<sup>5,6</sup> and nuclear reactor cladding.<sup>7–9</sup> SiC is also a natural material for armor due to the combination of high strength and low density.<sup>10–12</sup> However, the application of SiC in armor requires a deep understanding of its mechanical behavior under extreme conditions, commonly produced by shock loading. Shock studies on SiC and similar high strength ceramics have been extensively reported and encompass experiments and continuum modeling.<sup>10,11,13–22</sup> The shock performance of SiC was previously compared to that of B<sub>4</sub>C. While the Hugoniot elastic limit (HEL) of B<sub>4</sub>C, ~20 GPa, is higher than that of SiC, ~16 GPa, the latter shows an increasing strength with additional deformation in contrast to the former, which displays a severe strength loss.<sup>16</sup> Other experiments on SiC showed delayed failure<sup>23</sup> caused by interplay between plastic deformation and brittle failure modes.<sup>24</sup> An important piece of information is the shock Hugoniot which has been evaluated for SiC at pressures up to 160 GPa,<sup>25–27</sup> indicating a pressure induced transition at ~105 GPa. The evolution of shock waves was investigated in SiC rods,<sup>28</sup> indicating propagation of longitudinal waves at ~11 km/s in agreement with plate impact experiments.<sup>29</sup>

To this point, there is scarce atomistic modeling of shock loading on SiC, which is needed to complement the available experimental data and further our understanding of the dynamic behavior of SiC under extreme conditions. Previously, a combination of experiments and atomistic modeling was employed to describe the general trends of the

generation and propagation of shock waves and the shock induced fracture dynamics on SiC.<sup>30</sup> However, there is much more to be investigated. For instance, atomistic insights could clarify the shock induced structural transformation, the presence and character of plastic deformations, and the effect of crystal orientation and grain boundaries. Molecular dynamics (MD) simulations of plane shock loading have been widely used to investigate materials under extreme conditions and are an ideal tool for that purpose.<sup>31–35</sup> Large scale MD simulations of shock, allowing the modeling of much larger million atom systems, present an innovative dimension for the description of shock phenomena, narrowing the gap between experimental studies and microscopic descriptions of shock phenomena.<sup>36–38</sup> Nonetheless, realistic MD simulations of shock in ceramics are limited.<sup>39–41</sup> In addition to the SiC simulations performed earlier,<sup>30</sup> atomistic modeling of shock on SiC was performed using a Tersoff potential.<sup>42</sup> It demonstrated the formation of split shock waves and the generation of elastic, plastic, and transformation waves under increasingly intensive shocks. However, many questions remain unanswered, and a realistic description of experimental shock features is still lacking. For instance, the Tersoff potential used in the previous work on SiC<sup>42</sup> is unable to describe properly the high pressure phase of SiC and therefore unable to describe accurately the shock induced structural phase transformation from the low pressure zinc blend to the high pressure rock-salt.<sup>43,44</sup> Furthermore, Tersoff potentials overestimate the shock stress, shear stress, wave velocity, and temperature in SiC. In addition, SiC is a highly anisotropic material, and the shock response along different crystallographic directions should be properly described, as well as the effect of grain boundaries.

<sup>a)</sup>E-mail: branicio@usc.edu

In this work, MD is used to investigate the behavior of SiC under plane shock loading, considering explicitly the effects of low index crystallographic directions and grain boundaries. The atomic forces are derived from an effective many-body force field which was validated by an excellent agreement of its predictions with experimental elastic constants, melting temperature, vibrational density of states, and specific heat.<sup>44</sup> A more stringent validation of the potential is provided by the zinc blend-to-rock salt structural phase transition, which is reported in experiments and quantum mechanics simulations<sup>45</sup> to occur at  $\sim 100$  GPa.<sup>43,44</sup> This force field has been used to describe SiC fracture dynamics<sup>46</sup> and high strain-rate deformation of nanowires.<sup>47</sup> The same force field form has also been applied to describe the mechanical behavior of similar high strength ceramics such as AlN<sup>39,48,49</sup> and Al<sub>2</sub>O<sub>3</sub>.<sup>41,50,51</sup> The ability of the potential to accurately describe the response of SiC to extreme conditions was previously demonstrated by investigating the shock induced ductility in projectile impacts.<sup>52</sup>

Plane shock loading MD simulations are performed on SiC slabs with dimensions of  $\sim 12 \times 12 \times 200$  nm<sup>3</sup>, containing about three million atoms. Simulations are performed on both mono- and nano-crystalline 3C-SiC (nc-SiC) samples. Shock on monocrystalline samples is performed along the  $\langle 001 \rangle$ ,  $\langle 110 \rangle$ , and  $\langle 111 \rangle$  directions. The long system slab dimension, chosen as the  $z$ -direction, is aligned with the impact direction to allow the propagation of shock waves across the system for up to 18 ps. nc-SiC samples with an average grain size of  $d = 5$  nm and 10 nm are generated using the Voronoi tessellation method<sup>53–55</sup> and annealed to relax grain boundaries and minimize residual stresses.<sup>56</sup> Periodic boundary conditions are applied along the  $x$  and  $y$  directions and free surfaces along the impact  $z$  direction. The particle velocity  $u_p$ , which is the impact velocity, is chosen to be in the wide range of 0.1–6.0 km/s to access all shock regimes and induce stresses as high as 280 GPa. Simulations are done at  $T = 10$  K to minimize temperature fluctuations in the shock profiles. Nonetheless, similar simulations at  $T = 300$  K were performed and resulted in similar shock behavior. The atomic equations of motion are integrated with a time step of 1 fs. Analyses of physical properties are carried out along the impact direction using bins 7.5 Å wide. The calculated shock profiles include properties such as stress and displacement in the  $xy$  plane, perpendicular to the impact direction.

The shock Hugoniot calculated from all simulations is displayed in Fig. 1. The calculated shock response data, shown in solid symbols, can be divided into three regimes, elastic, plastic, and transformation, which agree very well with the experimental data<sup>25–27</sup> shown in open symbols. The anisotropic behavior of the 3C-SiC single crystals is highlighted by the shock Hugoniot simulated along  $\langle 001 \rangle$ ,  $\langle 110 \rangle$ , and  $\langle 111 \rangle$  and in the isotropic nc-SiC samples.

For monocrystalline SiC, wave configurations are well-defined. For  $u_p < 1.5$ – $2.25$  km/s, longitudinal elastic waves are generated. For  $\sim 1.5$ – $2.25 < u_p \leq 2.4$ – $2.5$  km/s, a plastic wave coexists with a faster elastic precursor. From  $\sim 2.4$  to  $2.5 < u_p < 5$  km/s, a structural-phase-transformation coexists with an elastic precursor. From  $\sim 5$  to 6 km/s onwards, a single overdriven wave is generated. In contrast, the shock response of the 5 nm grain size nc-SiC sample presents a

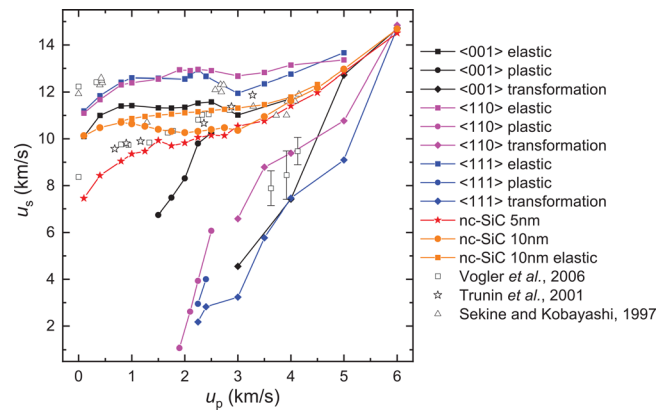


FIG. 1. Shock Hugoniot of 3C-SiC along low-index crystallographic directions and for nanocrystalline samples, nc-SiC, with 5 nm and 10 nm average grain sizes. Filled (open) symbols indicate simulation (experimental) data.

seamless Hugoniot with no explicit wave coexistence. However, shock on the 10 nm grain size nc-SiC sample indicates the presence of a two-wave structure in the intermediate regime  $0.8 < u_p < 4$  km/s with a plastic/structural phase transformation lagging behind the elastic shock front. The shock regimes identified from the simulations are in excellent agreement with the experimental data, considering the differences between modeling and experimental samples.

Elastic waves are generated for relatively weak shocks in SiC. Increasing the shock intensity, one reaches the end of the regime of purely elastic shock generation that indicates the Hugoniot elastic limit. The data in Fig. 1 indicate that the threshold  $u_p$  for this regime in monocrystalline samples is in the range of 1.5–2.25 km/s. However, signs of plasticity can be detected in the shock profiles in the range of  $u_p = 1.0$ – $2.0$  km/s, even though no well-defined plastic wave is generated in the short simulation time span. The results for 10 nm grain size nc-SiC indicate the onset of plasticity at  $u_p \sim 0.8$  km/s when the shock wave splitting begins. These results are in very good agreement with polycrystalline experimental data, which indicates the beginning of a region of compressed four-coordinated phase just beyond  $u_p \sim 0.5$  km/s. In Fig. 2, the atomic structure and shock profiles are shown for a typical plastic regime observed in the simulations. Figures 2(a)–2(c) show the data for the direction  $\langle 110 \rangle$  for impact at  $u_p = 2.5$  km/s. Plastic waves can take different forms and commonly involve dislocation plasticity. That is particularly the case for shocks on metallic materials. However, ceramics such as SiC have an outstanding resistance to dislocation plasticity. Single crystal simulations of plane shock loading on AlN have shown very restricted plastic deformation prior to structural phase transformation into high pressure phases.<sup>48</sup> A similar high resistance to dislocation plasticity is expected from SiC. However, SiC in its cubic phase (3C-SiC) has many available easy planes for dislocation glide. Previous simulations of the projectile impact on 3C-SiC have demonstrated that, in fact, under suitable conditions, a dense network of dislocation lines can be generated.<sup>52</sup> The results for shock on different crystallographic directions indicate that under plane shock conditions, 3C-SiC plastic deformation wave have predominantly deformation twinning as its primary deformation mode. The atomic structure at Fig. 2(a) shows a typical profile of deformation twinning present in

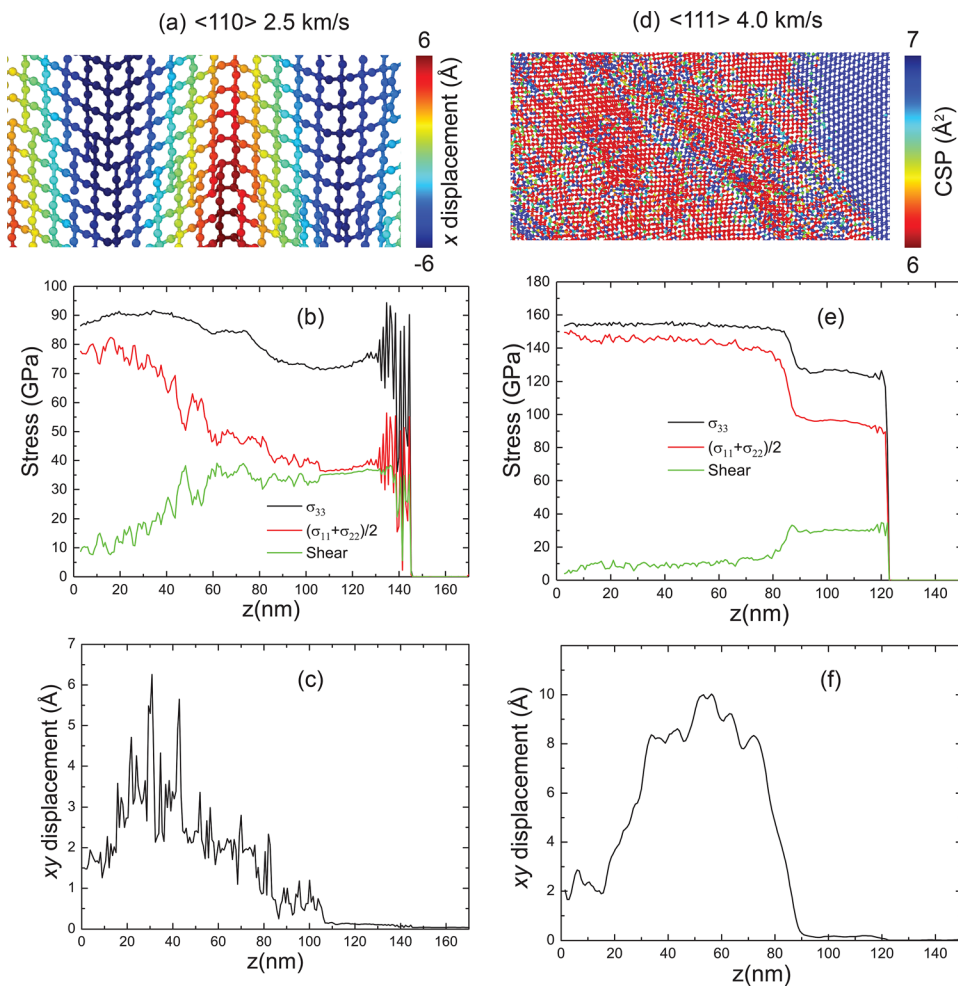


FIG. 2. Atomic structure and shock profiles of plastic and transformation waves. (a)–(c) Plastic wave along the  $\langle 110 \rangle$  direction for  $u_p = 2.5$  km/s. (a) Layer of atoms along the impact direction highlights the deformation twinning character of the plastic wave. Colors indicate displacement along one of the perpendicular directions to the shock propagation. (b) Stress profile indicating shear stress release at the shock front. (c)  $xy$  displacement profile indicating large atomic displacement generated by deformation twinning. (d)–(f) Transformation wave generated along the  $\langle 111 \rangle$  direction for  $u_p = 4.0$  km/s. (d) Layer of atoms along the impact direction indicates the structural phase transformation driving SiC from the low-pressure zinc blend (blue) to the high-pressure rock-salt phase (red). Colors indicate Centrosymmetry parameter (CSP) values. (e) Stress profile indicates the release of shear stress by the structural transformation wave. (f)  $xy$  displacement profile along the system, indicating that the transformation occurs by locally displacing atoms by up to  $10 \text{ \AA}$ .

the plastic waves with a dense pack of twins along the  $\langle 111 \rangle$  direction with the atomic displacement from initial positions highlighted, with  $x$  being the vertical direction in the figure. The plastic wave front is clearly defined by the stress profile shown in Fig. 2(b). The initial strong shear stress generated by the longitudinal elastic compression of  $\sim 36$  GPa is gradually released as the plastic deformation wave develops. The final shear stress calculated close to the impact surface is close to 10 GPa. A clear sign of plastic deformation is the sharp increase in atomic displacement on the plane perpendicular to the impact direction. Figure 2(c) indicates that at the plastic shock front, the average  $xy$  displacement increases sharply and continues to do so as the deformation twinning takes place in the system. Large average atomic displacements of over  $6 \text{ \AA}$  are observed in the plastically deformed region.

The Hugoniot displayed in Fig. 1 indicates that at  $\sim u_p = 3$  km/s, a transformation wave is generated and drives the system from the low-pressure zinc blend phase to the high pressure rock salt phase in agreement with experiments,<sup>27</sup> which indicates a transformation wave starting at  $\sim 3.6$  km/s. To illustrate the transformation wave, the atomic structure and shock profiles from the shock at  $u_p = 4.0$  km/s along the  $\langle 111 \rangle$  direction are shown in Figs. 2(d)–2(f). As can be seen in Fig. 2(d), the atomic structure undergoes a sharp transformation from the 4-coordinated zinc-blend phase (blue atoms) to the 6-coordinated phase rock salt (red atoms). Atoms' color is based on the value of the centrosymmetry parameter (CSP). The shock profiles shown in Figs. 2(e) and 2(f) indicate that

the shock front is sharp and the transformation generates a well-defined transformed state. The transformation releases most of the elastic wave shear stress. As shown in Fig. 2(e), the  $\sim 30$  GPa shear stress is quickly released by the transformation to a nearly hydrostatic state. The  $xy$  displacement shown in Fig. 2(f) indicates that the transformation displaces atoms sharply at the shock front by up to  $10 \text{ \AA}$ .

The nc-SiC Hugoniot does not indicate any sharp splitting of shock waves as displayed by monocrystalline models. Nonetheless, one can still distinguish three regimes for the two nc-SiC models considered. The thresholds for the plastic regime are located at  $u_p \sim 1.0$  km/s (10 nm) and 1.5 km/s (5 nm), while the threshold for the transformation regime is located at 3.0 km/s (10 nm) and 4.0 km/s (5 nm). Shear stress analysis, shown in Fig. 3(a), indicates shear accumulation below 1.25/1.5 km/s for 10/5 nm grain size models. That reveals the lack of release mechanisms and the presence of purely elastic (anelastic) compression of the sample. In contrast, from 1.25–1.5 km/s to 3.0–3.5 km/s, the shear stress is continuously released indicating the activation of plastic deformations consistent with the behavior observed for monocrystalline samples. At 4 km/s, a sudden increase in shear stress, which is then gradually released on increasing particle velocity, indicates a shift in release mechanisms, also consistent with the transformation wave described for shock on monocrystal SiC.

Two interesting questions are why there is no splitting in the shock Hugoniot observed for 5 nm nc-SiC and why the

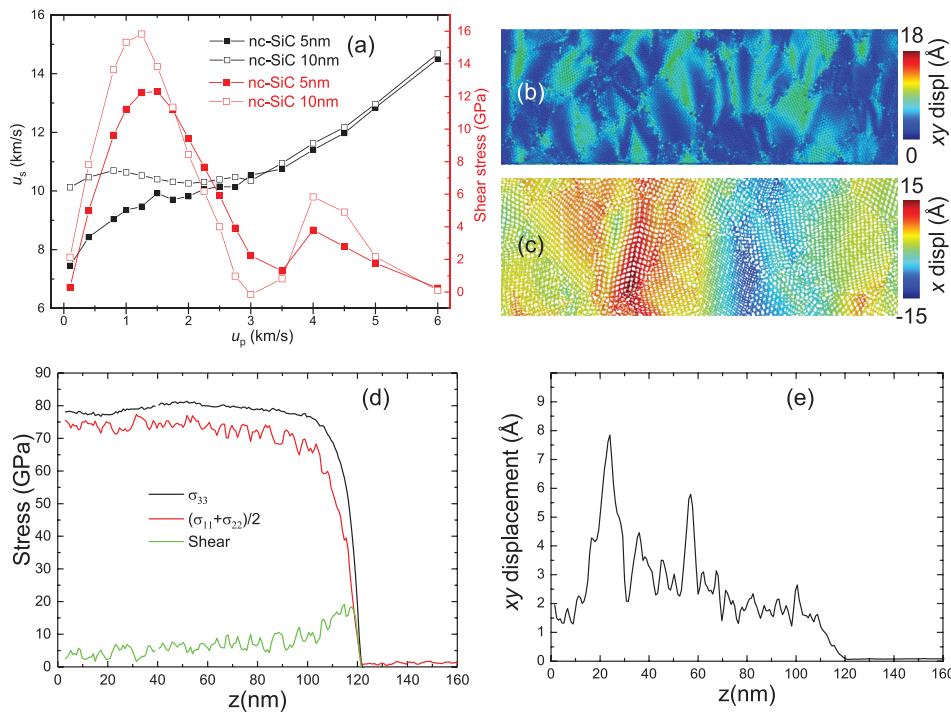


FIG. 3. Atomic structures and shock profiles of plastic deformation in the 5 nm nc-SiC for  $u_p = 2.5$  km/s. (a) Shock Hugoniot and shear stress also including data for the 10 nm nc-SiC model. (b) Layer of atoms along the impact direction highlighting plastic deformation at grain boundaries, e.g., grain boundary sliding. The color indicates displacement in the plane perpendicular to the impact direction. (c) Layer of atoms along the impact direction indicating also the presence of deformation twinning. Atoms are colored according to displacements perpendicular to the impact direction. (d) Stress profile indicating the release of shear stress at the shock front by the plastic deformations. (e)  $xy$  displacement profile indicating build-up of large atomic displacement in the plastic wave twinned regions.

Hugoniot curve follows almost perfectly the experimental curve corresponding to the plastic wave, see Fig. 1. One can answer both questions by noting the inherent structure of the 5 nm nanocrystalline sample. The grains in the 5 nm nc-SiC are substantially smaller than those in microcrystalline experimental samples. The fraction of softer amorphous interfaces is much larger as well at  $\sim 35\%$ .<sup>56</sup> When the experimental sample enters the plastic regime, the material increasingly accumulates defects and additional grain boundaries turning, on perspective, the structure closer to the nanocrystalline one. On the other hand, the plastic regime will not change dramatically the 5 nm nanocrystalline sample, given the already high density of interfaces and structural defects present. That is the main reason that the 5 nm nanocrystalline sample Hugoniot resembles that of the plastically deformed experimental sample and does not generate wave splits. Entering the structural transformation regime, the same argument is valid, and while the shear stress clearly indicates a change in release mechanisms, the Hugoniot indicates a relatively smooth increase in shock velocity. In contrast, the results for the 10 nm nc-SiC, which has a fraction of amorphous interfaces at  $\sim 18.5\%$ , show a split wave structure with a clear elastic shock front precursor. The shock profile however does not indicate a clearly defined profile of elastic, plastic, and transformation waves. Instead, a fuzzy wave front is formed with the particle velocity, density, and stress ramping up to steady state values over a wide wave front up to  $600 \text{ \AA}$  at  $u_p \sim 2.0$  km/s.

An intriguing aspect of the plastic wave in nc-SiC is that it activates different deformation mechanisms of the monocrystalline models. As shown in Figs. 3(b) and 3(c), the plastic wave in nc-SiC uses two atomistic mechanisms: grain boundary sliding and deformation twinning. Grain boundary sliding at such a small average grain size material is expected to be an important deformation mode. Figure 3(b) shows that in fact the bulk of the plastic deformation present

in the plastic wave is generated at or closer to the interfaces as highlighted by the  $xy$  displacement. Nevertheless, while the bulk of the deformation occurs at interfaces, deformation twinning is still active and takes place inside grains, as shown in Fig. 3(c). The 5 nm nc-SiC profiles of the plastic deformation, shown in Figs. 3(d) and 3(e) for  $u_p = 2.5$  km/s, clearly indicate an absence of wave splitting and a sharp plastic wave front. The stress profile shown in Fig. 3(d) indicates that the shear stress that is built quickly at the shock front is gradually released as the plastic wave develops until a nearly hydrostatic state is reached. The  $xy$  displacement for 5 nm nc-SiC, shown in Fig. 3(e), shows a highly inhomogeneous distribution of values between  $\sim 2$  and  $8 \text{ \AA}$ , which is a result of the combination of grain boundary sliding and deformation twinning. The results for the 10 nm nc-SiC while similar indicate a shock front width of  $\sim 450 \text{ \AA}$ , instead

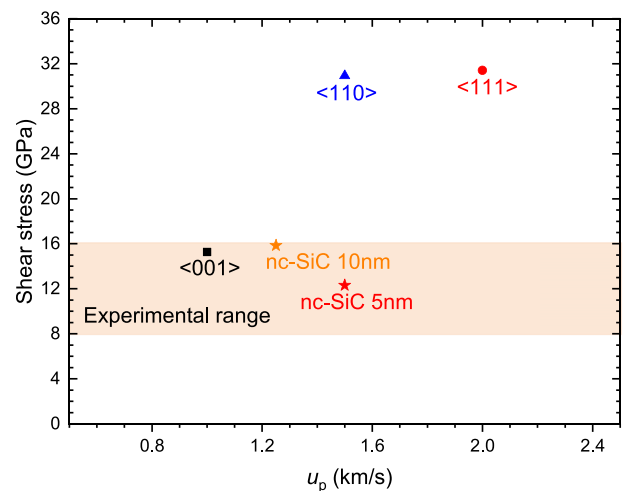


FIG. 4. Shear strengths for mono- and nano-crystalline SiC. The experimental range of reported values is plotted for reference.

of the sharp  $\sim 200 \text{ \AA}$  wave front shown in Fig. 3(d) for the 5 nm nc-SiC.

An important result from this study is the estimation of the strength of SiC from the calculated shear stress at the Hugoniot elastic limit. The strengths calculated for monocrystalline SiC are shown in Fig. 4, i.e., 15.2, 31.4, and 30.9 GPa along  $\langle 001 \rangle$ ,  $\langle 111 \rangle$ , and  $\langle 110 \rangle$  and 12.3 and 15.8 GPa for 5 nm and 10 nm nc-SiC. The results are in excellent agreement with the values measured experimentally<sup>27–29</sup> in the range of 8–16 GPa. The nc-SiC strength agrees very well in face of the expected loss of strength due to the softer interface material which constitutes a large fraction of the nanocrystalline samples.

This work was supported as part of the Computational Materials Sciences Program funded by the U.S. Department of Energy, Office of Science, Basic Energy Sciences, under Award No. DE-SC00014607.

- <sup>1</sup>M. A. Capano and R. J. Trew, *MRS Bull.* **22**, 19 (1997).
- <sup>2</sup>S. Wang, S. Dhar, S. R. Wang, A. C. Ahyi, A. Franceschetti, J. R. Williams, L. C. Feldman, and S. T. Pantelides, *Phys. Rev. Lett.* **98**, 026101 (2007).
- <sup>3</sup>W. Aiguo and H. J. Rack, *Wear* **146**, 337 (1991).
- <sup>4</sup>J.-C. Zhao and J. H. Westbrook, *MRS Bull.* **28**, 622 (2003).
- <sup>5</sup>F. E. Kennedy, A. C. Balbahadur, and D. S. Lashmore, *Wear* **203–204**, 715 (1997).
- <sup>6</sup>S. Fan, L. Zhang, Y. Xu, L. Cheng, G. Tian, S. Ke, F. Xu, and H. Liu, *Compos. Sci. Technol.* **68**, 3002 (2008).
- <sup>7</sup>H. Ko, A. Kaczmarowski, I. Szlufarska, and D. Morgan, *J. Nucl. Mater.* **492**, 62 (2017).
- <sup>8</sup>Y. Katoh, L. L. Snead, I. Szlufarska, and W. J. Weber, *Curr. Opin. Solid State Mater. Sci.* **16**, 143 (2012).
- <sup>9</sup>J. Deng, H. Ko, P. Demkowicz, D. Morgan, and I. Szlufarska, *J. Nucl. Mater.* **467**, 332 (2015).
- <sup>10</sup>D. L. Orphal, R. R. Franzen, A. C. Charters, T. L. Menna, and A. J. Piekutowski, *Int. J. Impact Eng.* **19**, 15 (1997).
- <sup>11</sup>T. J. Holmquist and G. R. Johnson, *J. Appl. Phys.* **91**, 5858 (2002).
- <sup>12</sup>M. Flinders, D. Ray, A. Anderson, and R. A. Cutler, *J. Am. Ceram. Soc.* **88**, 2217 (2005).
- <sup>13</sup>D. P. Dandekar, *J. Phys.* **IV 4**, C8-349 (1994).
- <sup>14</sup>D. P. Dandekar, A. Abbate, and J. Frankel, *J. Appl. Phys.* **76**, 4077 (1994).
- <sup>15</sup>V. A. Gorelskii, S. A. Zelepugin, and V. F. Tolkahev, *Chem. Phys. Rep.* **18**, 2211 (2000).
- <sup>16</sup>D. E. Grady, *J. Phys.* **IV 4**, C8-385 (1994).
- <sup>17</sup>D. E. Grady, *Mech. Mater.* **29**, 181 (1998).
- <sup>18</sup>J. W. Sweigle and D. E. Grady, *J. Appl. Phys.* **58**, 692 (1985).
- <sup>19</sup>A. Y. Vahora, P. Chaudhari, R. H. Joshi, N. K. Bhatt, and B. Y. Thakore, *AIP Conf. Proc.* **1591**, 84–85 (2014).
- <sup>20</sup>M. E. Kipp and D. E. Grady, *J. Phys.* **III 4**, C8-249 (1994).
- <sup>21</sup>M. Chen, J. W. McCauley, and K. J. Hemker, *Science* **299**, 1563 (2003).
- <sup>22</sup>G. R. Johnson, T. J. Holmquist, and S. R. Beissel, *J. Appl. Phys.* **94**, 1639 (2003).
- <sup>23</sup>N. Bourne, J. Millett, and I. Pickup, *J. Appl. Phys.* **81**, 6019 (1997).
- <sup>24</sup>J. C. F. Millett, N. K. Bourne, and D. P. Dandekar, *J. Appl. Phys.* **97**, 113513 (2005).
- <sup>25</sup>R. F. Trunin, L. F. Gudarenko, M. V. Zhernokletov, and G. V. Simakov, *Experimental Data on Shock Compression and Adiabatic Expansion of Condensed Matter* (Russian Federal Nuclear Center - VNIIEF, Sarov - Russia, 2001).
- <sup>26</sup>T. Sekine and T. Kobayashi, *Phys. Rev. B* **55**, 8034 (1997).
- <sup>27</sup>T. J. Vogler, W. D. Reinhart, L. C. Chhabildas, and D. P. Dandekar, *J. Appl. Phys.* **99**, 23512 (2006).
- <sup>28</sup>I. A. Balagansky, A. I. Balagansky, S. V. Razorenov, and A. V. Utkin, *AIP Conf. Proc.* **845**, 835–838 (2006).
- <sup>29</sup>A. S. Savinykh, G. I. Kanel, S. V. Razorenov, and V. I. Rumyantsev, *Tech. Phys.* **58**, 973 (2013).
- <sup>30</sup>M. O. Steinhauser, K. Grass, E. Strassburger, and A. Blumen, *Int. J. Plast.* **25**, 161 (2009).
- <sup>31</sup>B. L. Holian and G. K. Straub, *Phys. Rev. Lett.* **43**, 1598 (1979).
- <sup>32</sup>D. Brenner, D. Robertson, M. Elert, and C. White, *Phys. Rev. Lett.* **76**, 2202 (1996).
- <sup>33</sup>M. Vedadi, A. Choubey, K. Nomura, R. K. Kalia, A. Nakano, P. Vashishta, and A. C. T. van Duin, *Phys. Rev. Lett.* **105**, 014503 (2010).
- <sup>34</sup>K. Nomura, R. K. Kalia, A. Nakano, P. Vashishta, and A. C. T. van Duin, *Appl. Phys. Lett.* **101**, 073108 (2012).
- <sup>35</sup>S. C. Tiwari, K. Nomura, R. K. Kalia, A. Nakano, and P. Vashishta, *J. Phys. Chem. C* **121**, 16029 (2017).
- <sup>36</sup>T. Germann, B. Holian, P. Lomdahl, and R. Ravelo, *Phys. Rev. Lett.* **84**, 5351 (2000).
- <sup>37</sup>E. M. Bringa, J. U. Cazamias, P. Erhart, J. Stölken, N. Tanushev, B. D. Wirth, R. E. Rudd, and M. J. Caturia, *J. Appl. Phys.* **96**, 3793 (2004).
- <sup>38</sup>N. Gunkelmann, D. R. Tramontina, E. M. Bringa, and H. M. Urbassek, *New J. Phys.* **16**, 93032 (2014).
- <sup>39</sup>P. S. Branicio, R. K. Kalia, A. Nakano, P. Vashishta, F. Shimojo, and J. P. Rino, *J. Mech. Phys. Solids* **56**, 1955 (2008).
- <sup>40</sup>P. S. Branicio, M. H. Jhon, and D. J. Srolovitz, *J. Mater. Res.* **27**, 619 (2012).
- <sup>41</sup>C. Zhang, R. K. Kalia, A. Nakano, P. Vashishta, and P. S. Branicio, *J. Appl. Phys.* **103**, 083508 (2008).
- <sup>42</sup>W. H. Lee, X. H. Yao, W. R. Jian, and Q. Han, *Comput. Mater. Sci.* **98**, 297 (2015).
- <sup>43</sup>F. Shimojo, I. Ebbsjö, R. Kalia, A. Nakano, J. Rino, and P. Vashishta, *Phys. Rev. Lett.* **84**, 3338 (2000).
- <sup>44</sup>P. Vashishta, R. K. Kalia, A. Nakano, and J. P. Rino, *J. Appl. Phys.* **101**, 103515 (2007).
- <sup>45</sup>W. Kohn and P. Vashishta, *Theory Inhomogeneous Electron Gas* (Springer US, Boston, MA, 1983), pp. 79–147.
- <sup>46</sup>H. Kikuchi, R. K. Kalia, A. Nakano, P. Vashishta, P. S. Branicio, and F. Shimojo, *J. Appl. Phys.* **98**, 103524 (2005).
- <sup>47</sup>H. Tsuzuki, J. P. Rino, and P. S. Branicio, *J. Phys. D: Appl. Phys.* **44**, 55405 (2011).
- <sup>48</sup>P. S. Branicio, A. Nakano, R. K. Kalia, and P. Vashishta, *Int. J. Plast.* **51**, 122 (2013).
- <sup>49</sup>P. S. Branicio, R. K. Kalia, A. Nakano, and P. Vashishta, *Phys. Rev. Lett.* **96**, 065502 (2006).
- <sup>50</sup>C. Zhang, R. K. Kalia, A. Nakano, and P. Vashishta, *Appl. Phys. Lett.* **91**, 121911 (2007).
- <sup>51</sup>C. Zhang, R. K. Kalia, A. Nakano, and P. Vashishta, *Appl. Phys. Lett.* **91**, 071906 (2007).
- <sup>52</sup>P. S. Branicio, R. K. Kalia, A. Nakano, and P. Vashishta, *Appl. Phys. Lett.* **97**, 111903 (2010).
- <sup>53</sup>W. Brostow, J.-P. Dussault, and B. L. Fox, *J. Comput. Phys.* **29**, 81 (1978).
- <sup>54</sup>J. Finney, *J. Comput. Phys.* **32**, 137 (1979).
- <sup>55</sup>M. Tanemura, T. Ogawa, and N. Ogita, *J. Comput. Phys.* **51**, 191 (1983).
- <sup>56</sup>J. Y. Zhang, Z. D. Sha, P. S. Branicio, Y. W. Zhang, V. Sorkin, Q. X. Pei, and D. J. Srolovitz, *Scr. Mater.* **69**, 525 (2013).